

USE OF PARTIAL DISCHARGES MEASUREMENTS AND VIDEO RECORDINGS TO INVESTIGATE THE INFLUENCE OF RELATIVE HUMIDITY ON ZINC OXIDE SUBJECTED TO HIGH ELECTRIC FIELDS

Jean-François Fagnard^{1*}, Laurent Boilet², Jean-Pierre Erauw², François Henrotte³, Christophe Geuzaine³, Bénédicte Vertruyen⁴ and Philippe Vanderbemden¹

¹ *Electronics, Microsystems, Measurements, and Instrumentation (EMMI), Department of Electrical Engineering and Computer Science Montefiore Institute, University of Liege, 4000 Liège, Belgium*

² *Belgian Ceramic Research Centre, Avenue Gouverneur Cornez, 4, 7000 Mons, Belgium*

³ *Applied and Computational Electromagnetics (ACE), Department of Electrical Engineering and Computer Science Montefiore Institute, University of Liege, 4000 Liège, Belgium*

⁴ *GREENMAT, CESAM Research Unit, University of Liege, 4000 Liège, Belgium*

* E-mail: JF.Fagnard@uliege.be

KEYWORDS: partial discharge, zinc oxide, high voltage, flash sintering

ABSTRACT

This study investigates the influence of humidity on the high voltage behaviour of zinc oxide porous pellets at room temperature, using the phase resolved partial discharge (PRPD) method. The experimental configuration corresponds to the one that would be used for flash sintering cylindrical ZnO pellets at low temperatures in possibly scalable conditions: planar Pt electrodes without Pt paste. The study explores the incubation period by increasing the 50 Hz AC electric field up to 8 kV cm^{-1} (applied by steps or with a continuous ramp) in an air atmosphere with varying relative humidity (RH). Experiments were repeated on several samples and showed that the maximum amplitude of PDs decreased while their number increased as the RH increased. With the support of video recording of the experiments, different characteristics in the PD pattern evolution with increasing AC voltage could be attributed to various locations between the electrodes, at the sample surface, or at the interface with the electrodes. By examining the PRPDs, it was possible to identify two distinct types of PDs having different thresholds of inception: one type corresponds to PDs occurring mostly at the triple junction 'ZnO-platinum-air' or in the ZnO-electrodes gap and depends strongly on the RH level and; the other type corresponds to electric arcs between the electrodes, with an inception threshold much less affected by the RH level.

Supplementary material for this article is available online

(Some figures may appear in colour only in the online journal)

1. Introduction

The electric behaviour of zinc oxide (ZnO) is a subject of significant interest owing to the engineering applications of ZnO ceramics, such as varistors [1, 2], surge arresters [3], and insulating materials in electrical power systems [4, 5].

An attractive characteristic of zinc oxide is that it can be densified efficiently by flash sintering, an innovative technique developed since 2010 [6]. Flash sintering relies on applying an electric field during the heat treatment, in order to reduce significantly sintering temperatures and times [6-8]. Successful densification of ZnO was first demonstrated for an electric field applied at relatively high temperature [8-14] but recent works report that flash sintering of ZnO can also occur at room temperature [15-19]. This property opens up remarkable prospects in terms of energy savings. Although the physical mechanisms are still under debate [15, 19, 20], the common characteristics of flash sintering at room temperature are (i) the need of relatively high electric fields ($> 2.8 \text{ kV cm}^{-1}$ in air), and (ii) the possibility to speed up the physical processes by using suitable composition [19] and pressure [17] for the gas atmosphere, combined with increased humidity levels.

So far, room temperature flash sintering of ZnO has mostly been studied on small samples with 'dog-bone' shape (15 mm length, $\sim 6 \text{ mm}^2$ cross-section); using conductive silver paste to achieve optimal contact between platinum wires and the ZnO compacted powder [15, 17]. However, Ag or Pt paste contacts are not a suitable configuration when considering the scaling up of the technique to realistic samples of larger size, because of the cost and the difficulty to efficiently remove the Ag or Pt paste.

The purpose of the present work is to investigate the room temperature electric behaviour of ZnO ceramics subjected to high electric fields using planar Pt electrodes pressed against the sample, without any Ag or Pt paste. The focus is on the measurement of the partial discharges (PD) for various humidity levels. PDs are short ($\sim 1 \mu\text{s}$), localized electric discharges occurring either in the volume of the sample, along its surface or at any imperfect contact between the electrodes and the sample. Whether PDs occurring in the volume of the sample can be helpful to the flash sintering process itself is an open question. It is well-known that repetitive PDs in insulating materials can result in long-term damages since the released energy can cause a rapid heating and ultimately dielectric breakdown [21-24]. Measurements of PDs are commonly used in electrical engineering to assess the degradation and aging of high-voltage insulators [25-29], but the method has not yet been broadly adopted for ceramic materials [30-34]. In the context of flash sintering, PD measurements were recently shown to be an efficient method to characterize the quality and number of the electrode/sample contact areas when no Pt paste was used to sinter Y-stabilised zirconia (YSZ) above 250°C [35]. For (close to) room temperature flash sintering, relative humidity (RH) can be expected to be a highly relevant parameter, since it affects the electrical properties and breakdown characteristics of ceramics [36-38]. Because of its sensitivity to RH [39, 40], ZnO is a particularly interesting case to study the interplay between humidity, the occurrence of flashover

and the corresponding PD patterns, in order to improve their synthesis process under high electric field but also to optimize their performance and ensure their longevity in various engineering applications.

In the present work dealing with experiments at room temperature, we investigated how RH modified the characteristics of the PDs occurring in uncoated ZnO ceramics when they were placed in flash sintering conditions. We focused on the physical phenomena occurring in the (sometimes long) time interval before rapid densification occurs, i.e. the so-called 'incubation period' [41]. Several of our PD experiments were also combined with simultaneous video recordings, so that quantitative information from PD measurements can be compared to visually-observed surface flashovers.

2. Materials and methods

2.1. SAMPLE PREPARATION

High purity commercial ZnO powder (ZaNo20, Evercare) was dry-pressed into cylindrical pellets and pre-sintered at 550°C for 1 h (with heating and cooling rate of 5°C min⁻¹) to improve their mechanical resistance, yielding so-called 'green' pellets. The pellet for the impedance spectroscopy measurements had a thickness of 1.1 mm and a diameter of 25 mm. The pellets for all the high voltage (HV) experiments had a thickness of ~3.5 mm and a diameter of ~8 mm (see table 1) and a relative density of ~70% which was not affected by the PD experiments.

2.2. IMPEDANCE SPECTROSCOPY MEASUREMENTS

Impedance spectroscopy measurements were carried out under 30 mv rms without DC bias using a Solartron 1260 impedance gain-phase analyser with a Dielectric Interface 1296 in the frequency region of 1 Hz to 9.5 MHz. A climate chamber (Mettler HPP 108) was used to control the temperature and the RH between 5°C and 70°C and 10%- 90%, respectively; the achievable RH range varies with temperature. The electrical connections were made of silver paste and a guarded electrode configuration was used (diameter of 19 mm). All impedance spectroscopy measurements were carried out on the same sample, which was kept for one night at each RH value (starting by the lowest one).

2.3. ELECTRODES AND EXPERIMENTAL SETUP FOR PDS MEASUREMENTS

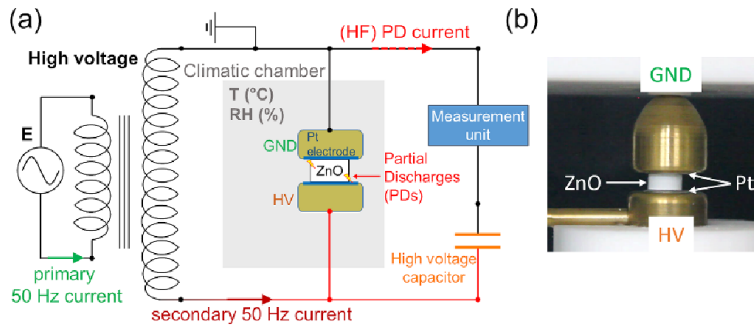
Each cylindrical ZnO sample was sandwiched between two platinum disc electrodes (thickness ~1 mm, diameter ~11 mm), supported by a brass and polytetrafluoroethylene (PTFE) structure as shown in figure 1(b). The structure was placed inside the Mettler HP108 climate chamber for stabilisation of both the temperature and the RH. All PDs experiments in this work were carried out at 35°C and RH levels of 10%RH, 50%RH or 90%RH. The climate chamber was grounded and the top electrode was connected to the ground. The bottom electrode was connected to the

secondary winding of the HV transformer with a 25 kV PTFE insulated cable via a hermetic connection through the wall of the climate chamber. A Canon EOS 550D camera was used to record videos of selected experiments.

Table 1. Dimensions of the measured samples, relative humidity levels at which experiments were carried out, and ID numbers of the recorded videos.

Sample	Diameter (mm)	Thickness (mm)	RH level (%)	Video ID
RH10-a	7.77	3.54	10	S1
RH50-a	7.70	3.23	50	S2
RH50-b	7.69	3.63	50	S4
RH50-c	7.75	3.25	50	—
RH90-a	7.72	3.38	90	S3
RH90-b	7.62	3.38	90	S5

Figure 1. (a) Experimental setup for partial discharges measurements in the climate chamber. (b) ZnO sample placed between platinum disc electrodes, supported by a brass and PTFE structure. The high voltage was applied to the bottom electrode and the ground was connected to the upper electrode. The climate chamber was grounded.



2.4. PDS DETECTION SYSTEM AND INSTRUMENTATION

A 50 Hz AC voltage (V) was applied to the samples through a HV transformer (1:240 ratio). The amplitude of V was increased either in successive steps up to a maximum value of $\sim 7-8$ kV, depending on the sample thickness, or as a continuous ramp (25 V s^{-1}). Coarse voltage steps were used up to 800 V and finer steps of 20 V (corresponding to average electric field steps of 60 V cm^{-1}) were used above 800 V. The RMS values of the voltage at 50 Hz and the current were measured at the primary winding of the HV transformer with HP 34 401 A multimeters and a Fluke i30s current probe.

PDs were measured using an Insulation Condition Monitoring (ICM) system from Power Diagnostix [42] described in more details in [35]. PD patterns in the frequency range 40–800 kHz were recorded during an acquisition time set to 30 s. A low-level detection threshold of 10 pC was used to reject

low-level noise signals. Preliminary experiments carried out on a cylinder of PTFE of similar dimensions (see appendix), proved that the PD patterns up to 8 kV cm^{-1} could be attributed to the physical behaviour of the ZnO sample and did not originate from other parts of the experimental setup.

In the following, each 'phase resolved' PD pattern, is plotted with a horizontal axis from 0° to 360° corresponding to the phase φ of the applied 50 Hz AC voltage; the positive (negative) polarity corresponds to phase angles between 0° and 180° (between 180° and 360°). The vertical axis is the amplitude q of the PD, in pC. During the duration of the acquisition, each measured PD becomes a point in this (φ - q) plane; the colour code (from grey to red to orange to yellow in logarithmic progression) reflects the number of PDs with similar characteristics of amplitude and phase. The sum of the amplitudes (taken in absolute value) of all PDs divided by the acquisition time (here 30 s) is defined as the average discharge current.

3. Results

Prior to measuring the PDs, we first characterised how the volume electrical conductivity of the green ZnO samples is affected by environmental conditions, using impedance spectroscopy measurements at various temperature and RH levels (section 3.1). We then move to PD measurements under high AC electric field, carried out at 35°C and three humidity levels (sections 3.2.1-3.2.4). Finally, PD measurements carried out when the AC field amplitude was increased continuously are compared to video recordings in section 3.3.

3.1. IMPEDANCE SPECTROSCOPY RESULTS

The DC volume electrical conductivity and the AC volume electrical conductivity at 50 Hz of a ZnO pellet submitted to different temperatures and RH levels were extracted from complex impedance data by considering the total electrical conductivity as the sum of σ_{DC} and σ_{AC} . According to Jonscher's law [43], the AC conductivity of many dielectric materials can be described by a power-law relationship with frequency, so that $\sigma_{\text{TOTAL}}(\omega) = \sigma_{\text{DC}} + \sigma_{\text{AC}} = \sigma_{\text{DC}} + A\omega^s$, where A is a constant, ω is the angular frequency, and s is the Jonscher exponent ($0 < s < 1$). Figure 2 shows the temperature and RH dependence of σ_{DC} (obtained from a fit by Jonscher's law in the low frequency range) and σ_{AC} at 50 Hz (the frequency of the applied voltage in the PDs experiments). Both increase with RH and temperature. At 35°C , σ_{AC} increases by a factor of 40 between 10%RH and 90%RH, significantly larger than the factor of 2.28 reported in [44] for dense ZnO between 5%RH and 98%RH. The larger value obtained in our measurements is likely due to the large porosity of the green samples.

Arrhenius plots were used to calculate activation energy values for the DC conductivity (between 0.75 eV and 0.78 eV) and AC conductivity (between 0.32 eV and 0.45 eV), as reported in table 2; note that the activation energies were not determined at 90%RH since only a 10°C temperature window was accessible experimentally. As a comparison, the activation energy for the DC electrical conductivity of dense ZnO in inert atmosphere was reported as 0.85 eV in [44].

The inset in figure 2 plots the temperature dependence of the Jonscher exponent s , which depends on the nature of the conductivity mechanism [45]. The decrease of s with increasing temperature was consistent with the carrier barrier hopping (CBR) model [46, 47], where $s = 1 - 6k_B T/W_m$ with k_B the Boltzmann constant and W_m the maximum barrier height. W_m values of 0.1 eV, 0.18 eV, 0.21 eV and 0.16 eV were obtained for 10%RH, 30%RH, 50%RH and 70%RH.

Figure 2. DC volume electrical conductivity (open symbols) and AC ($f = 50$ Hz) volume electrical conductivity (solid symbols) for temperature of 5°C, 15°C, 25°C, 35°C, 45°C, 55°C and 65°C and relative humidity of 10%RH, 30%RH, 50%RH, 70%RH and 90% RH. The lines are guides for the eye.

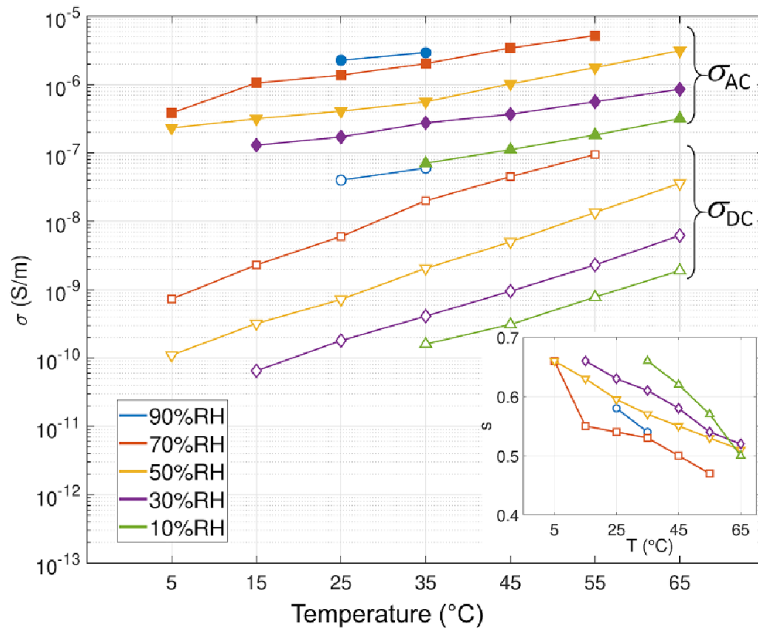


Table 2. Activation energies for the DC and the AC electrical conductivities calculated from impedance spectroscopy measurements on ZnO samples at various relative humidity values.

RH (%)	E_a (σ_{DC}) (eV)	E_a (σ_{AC}) (eV)
10	0.75	0.45
30	0.75	0.32
50	0.77	0.35
70	0.78	0.38

3.2. PHASE-RESOLVED PDS MEASUREMENTS

Now we turn to the experimental results on the green ZnO pellets subjected to electric fields increased in 30-second steps up to 7-8 kV cm⁻¹ at 35°C. The phase resolved partial discharge (PRPD) measurement mode was used in order to record in which part of the sinewave of the applied electric field the PD occur.

The complete series of PRPD patterns (between 100 and 150 for each experiment) are provided as supplementary information. In the following sub-sections, we show representative PRPD patterns selected along the average discharge current vs. average electric field curves to illustrate the emergence of groups of PDs, hereafter called ‘clusters’. Different cluster types display specificities regarding their phase location with respect to the voltage sinewave, the amplitude and number of PD, and their appearance or disappearance for certain values of the average electric field. The last sub-section shows plots of aggregated data in order to review the impact of relative humidity on the emergence of the PD clusters.

3.2.1. RESULTS AT 10%RH. Figure 3 shows the average discharge current curve and representative PRPD patterns collected at 10%RH on sample RH10-a. Below 2.5 kV cm^{-1} , PD activity was practically non-existent (see pattern ① in figure 3(b)). Starting from about 2.5 kV cm^{-1} , PD clusters appeared in the positive polarity of the voltage sinewave (see green triangles in patterns ② and ③ in figure 3(b)). This type of clusters, characterized by a broad dispersion in amplitude but located in narrow phase windows of $\sim 10^\circ$ (equivalent to time windows of $\sim 0.5 \text{ ms}$) will be called ‘vertical clusters’ in the following. These vertical clusters remained the only ones up to about 4 kV cm^{-1} ; the average discharge current in this range did not exceed 1 nA (considering a realistic threshold of 10 pA) due to the low number and amplitude of the PDs. Vertical clusters were also observed in the patterns collected under higher applied electric fields, with progressively higher PD amplitudes.

Above 4.05 kV cm^{-1} , another type of clusters appeared in the patterns, with broader phase distributions mostly centred on the maxima of the voltage sinewave (see pattern ④ in figure 3(b)). These clusters evolved into triangular distributions and the number of PDs increased rapidly (see pattern ⑤ in figure 3(b)), producing a sharp increase in the average discharge current reaching several tens of nA. Above 5.3 kV cm^{-1} , a new cluster centred on the positive polarity maximum of the voltage sinewave developed in the amplitude range between 50 pC and 300 pC (see pattern ⑥ in figure 3(b)—note the change in the y-axis scale). Starting from 5.7 kV cm^{-1} , yet another cluster of the same type developed at even higher amplitudes (from 400 pC to beyond 1000 pC —see patterns ⑦ and ⑧ in figure 3(b)).

These observations show that the PRPD method can be used in order to reveal two distinct families of PDs clusters in terms of amplitude and phase: thin vertical clusters and much wider clusters centred on the maxima of the voltage sinewave.

3.2.2. RESULTS AT 50%RH. Figure 4(a) shows results obtained under 50%RH for sample RH50-a. Two other samples (RH50-b and RH50-c) were measured under the same experimental conditions. At low electric fields, the missing points in the average discharge current plotted in figure 4 are due to the fact that no PD were detected, hence the average discharge current is zero and the points are not visible using the vertical logarithmic scale. The feature trends described hereafter were observed in all samples, with slight shifts in the quantitative values of electric field threshold and ranges of amplitudes, as expected due to the stochastic nature of PD activity.

Under 50%RH, vertical clusters appeared above 2.6 kV cm^{-1} , in the positive polarity and with very low amplitude ($< 20 \text{ pC}$ —see pattern ① in figure 4(a)). Vertical clusters were also observed in the

patterns collected under higher applied electric fields, with progressively higher PD amplitude reaching 200-300 pC in the 6-8 kV cm⁻¹ range (see pattern 4 in figure 4(a)).

Above 3.11 kV cm⁻¹, clusters centred on the maxima of the voltage sinewave started to appear (see pattern 2 in figure 4(a)) and, despite their low individual amplitude, collectively increased the average discharge current to 36.2 nA at 3.5 kV cm⁻¹ (to be compared to 0.7 nA for sample RH10-a). Clusters of PDs developed progressively at higher amplitudes: between 20 pC and 50 pC starting from 3.8 kV cm⁻¹ (see pattern 3 in figure 4(a)), and between 50 pC and 200 pC above 5 kV cm⁻¹. These new clusters partly or completely merged with the clusters at lower amplitudes.

The range between 5.5 kV cm⁻¹ and 8 kV cm⁻¹ was characterized by marked fluctuations in the number and amplitude of PDs, as reflected in the average discharge current curve. These fluctuations contrasted with the almost monotonous behaviour of sample RH10-a measured in 10%RH. A possible explanation of these fluctuations might arise from the increase probability of condensation of droplets of water at the surface of the sample despite the fact that the temperature inside the chamber is regulated to 35°C and therefore if any condensation appeared it should primarily occur on the climatic chamber walls and not at the centre of the climatic chamber. Another possible origin of the fluctuations might come from the active control of the RH level where water steam is intermittently injected inside the climatic chamber. This could induce some wet air flow convection and fluid mechanical turbulences around the sample. Finally, the presence of discharged induced flow is also possible [48, 49].

Figure 3. (a) Evolution of the average discharge current with respect to the average electric field up to 8 kV cm⁻¹ measured in 10%RH on sample RH10-a. (b) PRPD patterns obtained at the average electric field values labelled on figure (a). The so-called vertical clusters are identified with green arrows. The scale of the y-axis increases in pattern 6 and again for patterns 7 and 8.

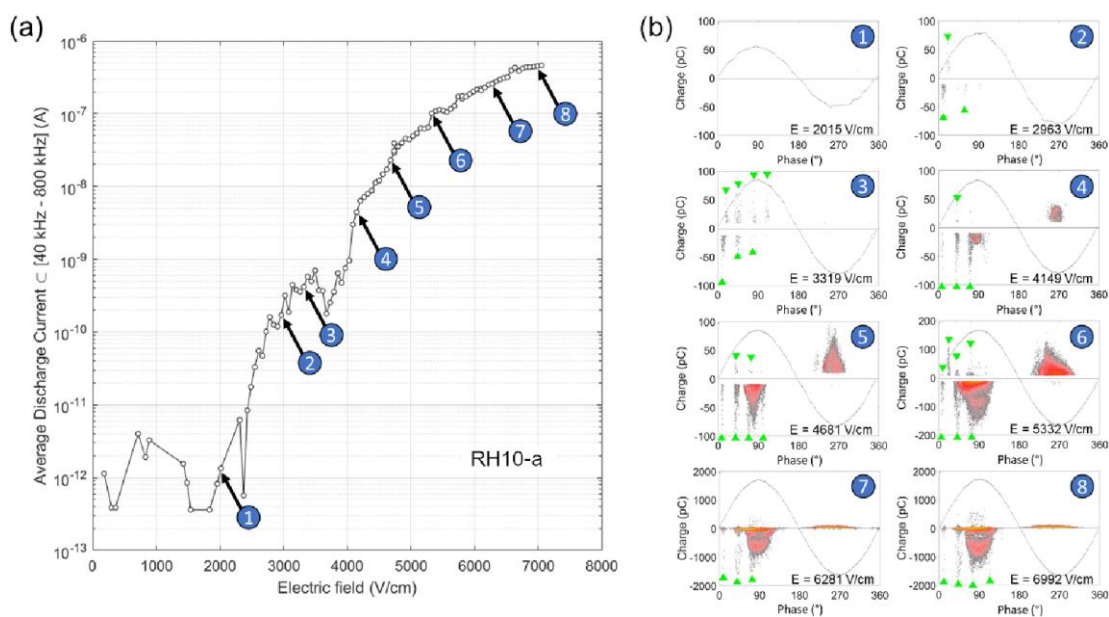
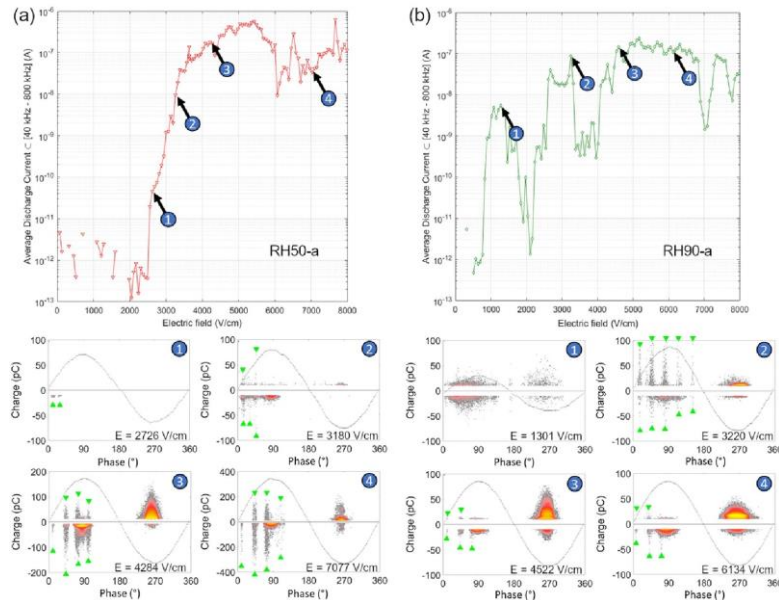


Figure 4. Evolution of the average discharge current measured (a) in 50%RH on sample RH50-a and (b) in 90%RH on sample RH90-a, with respect to the average electric field up to 8 kV cm^{-1} and PRPD patterns obtained at the average electric field values labelled by numbered circles. The vertical clusters are identified with green arrows. The scale of the y-axis increases in pattern ③ and again in pattern ④ for sample RH50-a.



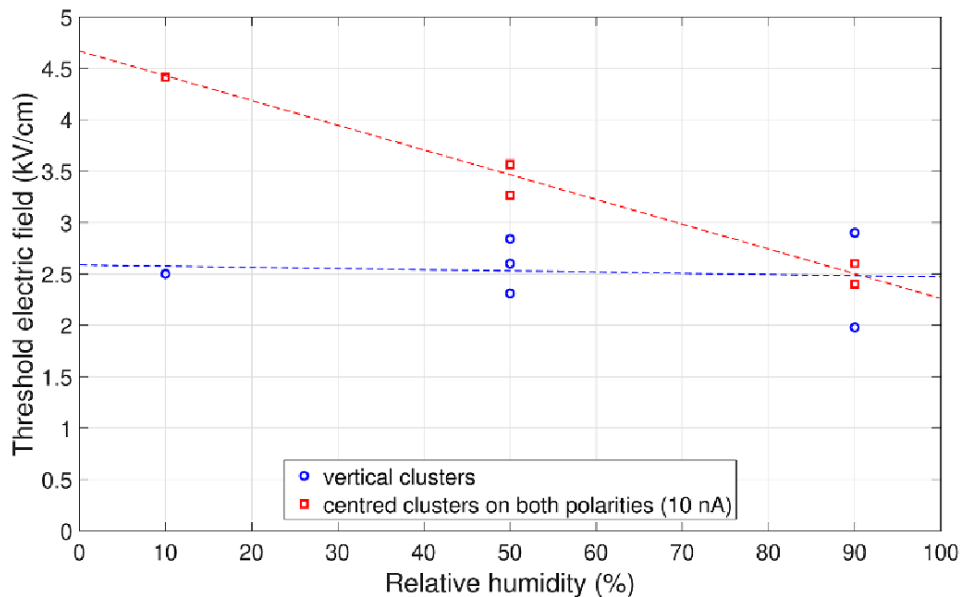
3.2.3. RESULTS AT 90%RH. Figure 4(b) shows results obtained under 90%RH for sample RH90-a. Another sample (RH90-b) was measured under the same experimental conditions. The feature trends described hereafter were observed for both samples, with slight shifts in the quantitative values of electric field threshold and ranges of amplitudes.

Under 90%RH, a new type of clusters was observed at comparatively low electric fields: between 0.8 kV cm^{-1} and 2 kV cm^{-1} , PDs of low amplitude ($< 50 \text{ pC}$) formed diffuse clusters located in the phase ranges where the voltage sinewave increased in amplitude (0° - 120° for the positive polarity and 180° - 300° for the negative polarity—see pattern ① in figure 4(b)). These clusters involved low (negative polarity) to moderate (positive polarity) numbers of PDs and resulted in a local maximum of the average discharge current, which reached several nA at 1.5 kV cm^{-1} before decreasing back to the noise level.

Clusters of low amplitude ($< 15 \text{ pC}$) centred on the maxima of the voltage sinewave (mostly in the negative polarity) started to emerge at 2.15 kV cm^{-1} , i.e. *before* the vertical clusters, which appeared at 2.9 kV cm^{-1} (see pattern ② in figure 4(b)). Above 4.1 kV cm^{-1} , further PDs centred on the maximum of the voltage sinewave appeared between 15 pC and 75 pC and merged with the primary cluster in the negative polarity (see patterns ③ and ④ in figure 4(b))

The high electric field range was characterized by even higher fluctuations than at 50%RH, with the average discharge current dropping from $\sim 100 \text{ nA}$ to $\sim 1 \text{ nA}$ between 3.2 kV cm^{-1} and 4 kV cm^{-1} and again around 6.8 kV cm^{-1} .

Figure 5. Threshold electric fields corresponding to the appearance of the vertical clusters and the clusters occurring in both polarities as a function of relative humidity leading to an average discharge current of 10 nA. The datapoints correspond to samples RH10-a, RH50-a, RH50-b, RH50-c, RH90-a and RH90-b.



3.2.4. COMPARISON OF THE AVERAGE CHARACTERISTICS AT VARIOUS RH VALUES. Figure 5 was built from the observations in figures 3 and 4 and the equivalent results for the additional samples RH50-b, RH50-c and RH90-b. The figure shows that the threshold value for the appearance of thin vertical clusters was only weakly affected by RH. On the contrary, the threshold for the appearance of clusters occurring in both polarities for values of the average discharge current equalling 10 nA decreases with increasing RH. The peak between 0.8 kV cm^{-1} and 2 kV cm^{-1} in the average discharge current was observed only at 90%RH and was not plotted in the figure.

Only a selection of PRPD patterns could be shown in the previous sections. In order to take advantage of the complete datasets, the distributions of several average characteristics are plotted in figure 6 as a function of the electric field steps and/or the phase windows: (i) the average discharge current, (ii) the number of PDs H_n , (iii) the mean amplitude of the PDs H_{qm} , and (iv) the maximum amplitude of the discharges H_{qm} . The graphs are shown in the same scales for all six samples (1 at 10%RH, 3 at 50%RH and 2 at 90%RH) to allow for easy comparison and to evaluate the reproducibility of the PD behaviour for samples measured in the same RH conditions.

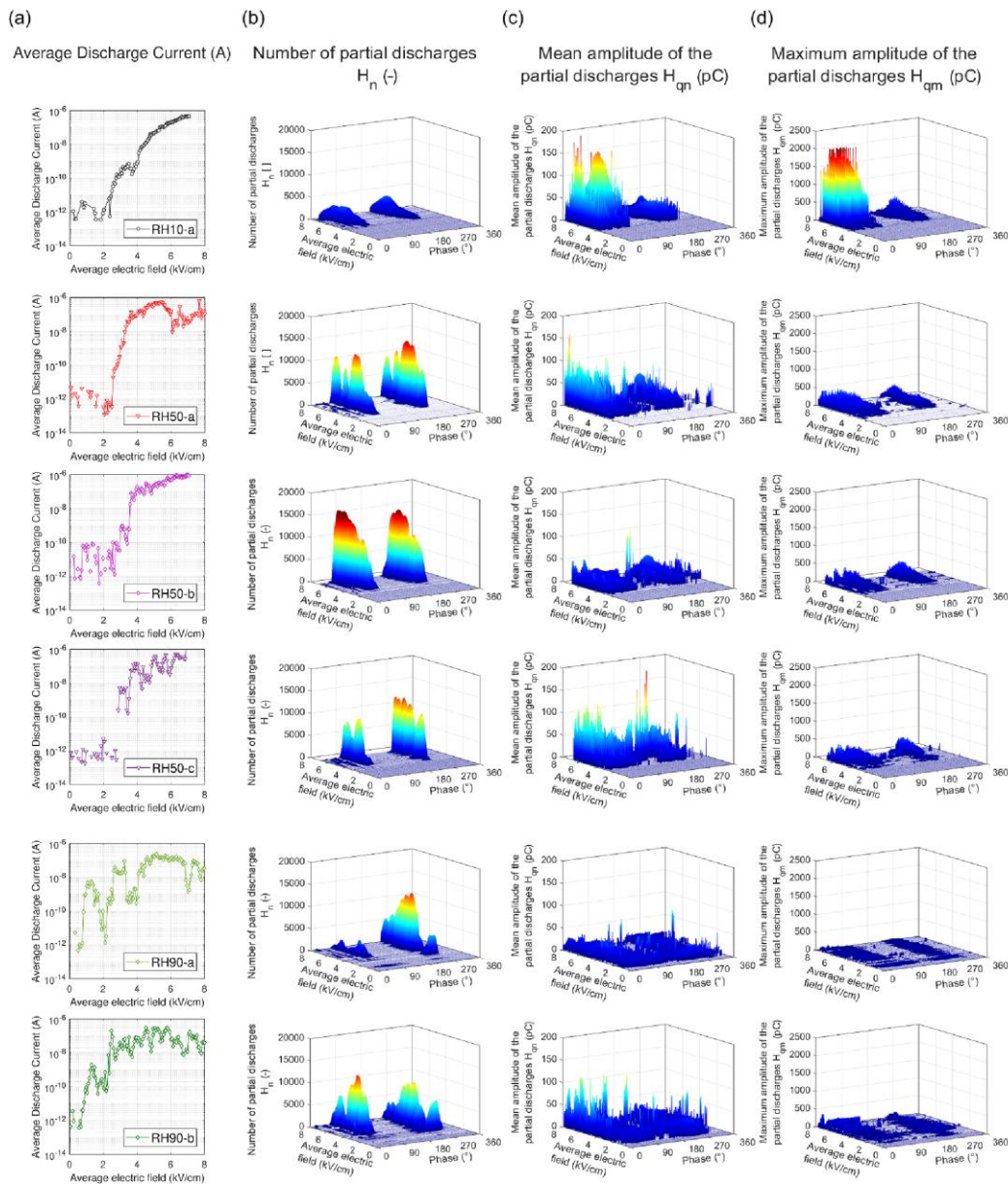
The similarity between the data for different samples measured at the same RH was clear enough to identify general trends for the influence of RH on the PD behaviour. Although we do not elude the difference in total PD counts, the most important point we wish to emphasize are the commonalities that these two samples have compared to those measured at lower RH levels.

In all cases, the PD numbers were highest around the maxima of the voltage sinewave (phase angles around 90° and 270°), with a broader distribution at 90%RH.

The influence of the RH could be seen in the PD numbers distribution, which extended to much higher values at 50%RH and 90%RH (between 10 000 and 15 000) than at 10%RH (below 3200).

Conversely, the maximum amplitudes of PDs recorded at 50%RH and 90%RH (below 400 pC) were much lower than at 10%RH (up to 2000 pC in the positive polarity). Therefore, the increase in the average discharge current at 10%RH was essentially due to the relatively few highamplitude PDs. At higher relative humidities (50%RH and 90%RH), the average discharge current resulted from the accumulation of large numbers of small-amplitude PDs. The fluctuations in the average discharge current were more significant for the samples where the distribution of PD numbers showed more irregular variations with respect to the average electric field.

Figure 6. Aggregated data extracted from the PRPD datasets collected on 1 sample at 10%RH, 3 samples at 50%RH and 2 samples at 90%RH: (a) average discharge current as a function of average electric field; (b)-(d) distributions of the number of partial discharges H_n , mean amplitude of the partial discharges H_{qn} and maximum amplitude of the partial discharges H_{qm} as a function of the average electric field ($\sim 60 \text{ V cm}^{-1}$ steps) and the phase of the voltage sinewave (256 phase windows of 1.4°). Note that the saturation visible in figure (d) is due to a few partial discharges reaching the full-scale (2000 pC) of the data acquisition system.

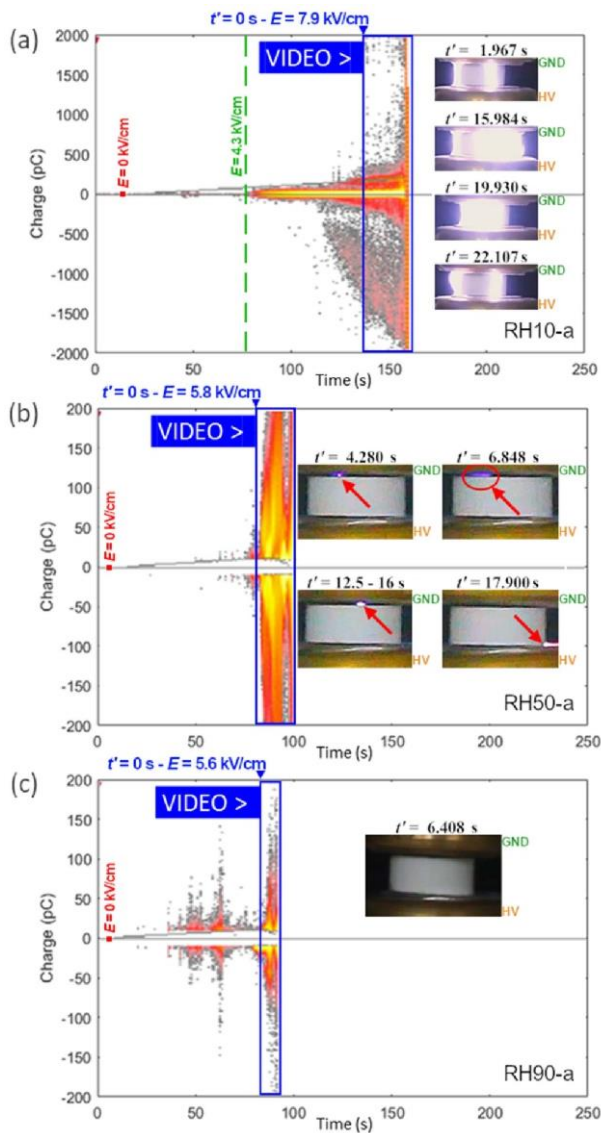


3.3. PD VS TIME AND VIDEO RECORDINGS

In a second experiment, each ZnO sample was subjected to an AC voltage whose amplitude V was increased as a continuous ramp (25 Vs^{-1}). When the 50 Hz current measured at the primary winding of the HV transformer reached 0.3 A (1.25 mA at the secondary winding of the HV transformer), the voltage was automatically reset to zero and the experiment was stopped.

During these fast experiments, the amplitude of the PDs was measured as a function of the elapsed time, as shown in figure 7 for the samples RH10-a, RH50-a and RH90-a. Videos were recorded during each experiment; the final section of each video (starting at the $t' = 0 \text{ s}$ mark in the graphs of figure 7) are provided as supplementary information.

Figure 7. Amplitude of the partial discharges measured during a 25 Vs^{-1} voltage ramp applied at 35°C and (a) 10%RH, (b) 50%RH and (c) 90%RH. Insets: Photographs extracted from the video during the experiments where the time is referred to the start time of each video (i.e. $t' = 0 \text{ s}$). Mentions of the HV and GND figure the electrical configuration of the sample.



In the following, the term ‘arc’ will be used to denote any visible electric events recorded by the camera by contrast to the ‘partial discharge’ term that corresponds to any electric event detected through electric measurements, i.e. the ICM system.

In figure 7(a) corresponding to sample RH10-a (please note the broader range of amplitude in this graph compared to graphs (b) and (c)), PDs between 50 pC and 100 pC emerged in both polarities when the average electric field reached 4.3 kV cm^{-1} (green line mark). Starting from 6 kV cm^{-1} , a separate high-amplitude cluster developed in the negative part of the graph, in agreement with what was observed in pattern ⑥ in figure 3(b). The video recording in supplementary material S1 starts at 7.9 kV cm^{-1} and shows the last 25 s of the experiment. Very brief electric arcs were observed between the electrodes along the side surface of the sample: about 10 arcs could be counted during the 15 s following the first one at $t' = 1.967 \text{ s}$, then 7 arcs separated by approximately one second between $t' = 15 \text{ s}$ and $t' = 20 \text{ s}$ and finally a burst of about 15 arcs in less than two seconds just before the current- controlled end of the experiment. This burst was correlated with the PD measurement above 9.6 kV cm^{-1} , where the PD amplitudes suddenly increased up to more than 2000 pC. In figure 7(a), the saturation of the PD pattern visible at the end of the experiment results from charge amplitudes reaching the full-scale of the PD acquisition system (2000 pC). The snapshots shown in the inset of figure 7(a) illustrate that the majority of the arcs appeared to be pinned to the sample close to its lateral surface; occasionally several arcs combined to completely mask the lateral surface of the sample as shown in the $t' = 19.930 \text{ s}$ inset of figure 7(a).

In figure 7(b) corresponding to sample RH50-a, PDs of very low amplitude (below 50 pC) emerged around 4.5 kV cm^{-1} and were quickly followed by more intense PDs reaching more than 200 pC. A brief drop in the PD amplitude took place just before the final rush preceding the end of the experiment. The video recording in supplementary material S2 starts at 5.8 kV cm^{-1} and shows the last 20 s of the experiment. Some snapshots are shown as insets of figure 7(b). Narrow electric arcs happened between $t' = 3 \text{ s}$ and $t' = 6 \text{ s}$ at the interface between the upper electrode (ground) and the sample. These narrow arcs turned into a purple glow lasting from $t' = 6 \text{ s}$ to $t' = 11 \text{ s}$, probably due to discharges in close succession. From $t' = 12 \text{ s}$ to $t' = 16 \text{ s}$, narrow arcs gathered into a broader arc, which remained stable for a few seconds before fading away. Finally, between $t' = 17 \text{ s}$ and $t' = 18.5 \text{ s}$, reflected light appeared at the bottom right of the sample, suggesting that a quite intense arc was happening behind the sample and was thus not visible on the video. In figure 7(b), the saturation of the PD pattern visible at the end of the experiment results from charge amplitudes reaching the full-scale of the PD acquisition system (200 pC).

In the video recording of the last 5 s of the same experiment carried out on sample RH50-b (supplementary information S4), the arc occurred at the front of the sample and a series of snapshots from the video are shown in figure 8. At $t' = 1.889 \text{ s}$ (average electric field of 5 kV cm^{-1}), small arcs were observed between the HV electrode and the sample. At $t' = 1.901 \text{ s}$, a bright arc connected the two electrodes along the lateral surface of the sample. It then became less intense ($t' = 2.185 \text{ s}$) before dividing into two arcs, each of them connecting one electrode with the sample ($t' = 2.209 \text{ s}$). These arcs gradually moved towards the right of the sample, with occasional sparks

between them (e.g. $t' = 2.934$ s, $t' = 3.368$ s). The arcs initially present between the HV electrode and the sample persisted throughout this period while additional arcs appeared later between the ground electrode and the sample (e.g. $t' = 3.526$ s, $t' = 3.664$ s). Once the threshold for the current in the primary winding of the transformer was reached ($t' = 4.431$ s), the voltage dropped to zero, and the arc was extinguished.

In figure 7(c) corresponding to sample RH90-a, PDs of low amplitude (below 100 pC) emerged then disappeared between 25 s (1 kV cm^{-1}) and 70 s (2.5 kV cm^{-1}).

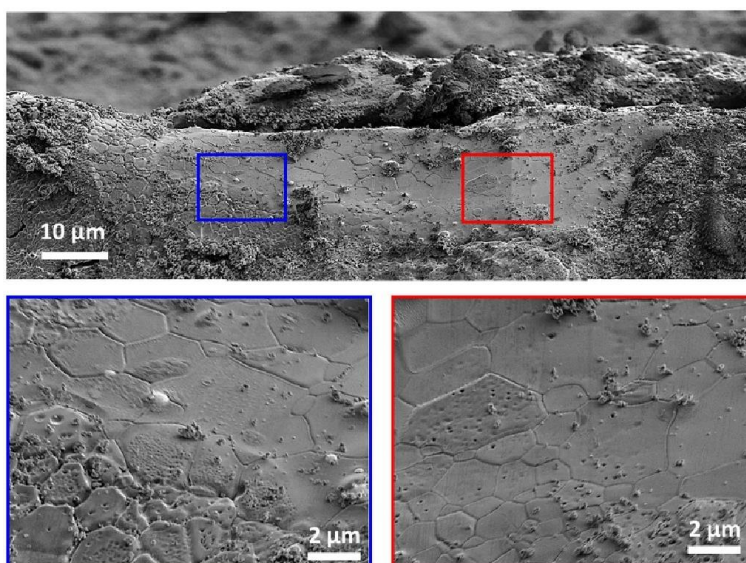
Above 4.5 kV cm^{-1} (i.e. after 75 s), PDs with amplitudes extending to 200 pC were recorded before the end of the experiment. Supplementary information S4 and S5 show the last 10 s of the experiments on sample RH90-a and RH90-b. The only optical event that could be observed was a slight purple glow at the right corner of the sample in contact with the HV electrode, between $t' = 5$ s and $t' = 6.3$ s for sample RH90-b.

Due to the sensitivity of the measurement setup (designed for PD detection), all the experiments reported above were limited to what would be the incubation period of a flash sintering procedure. As a result, no macroscopic densification of the pellets was observed; however, localized areas of surface densification were detected by scanning electron microscopy after the experiments performed at 50%RH or 90%RH. The micrographs displaying the most advanced sintering state were collected after the experiments at 90%RH (figure 9), close to the edge of the samples. The micrographs in figure 9 show the local development of large well-connected hexagonal grains in sample RH90-a. No evidence of such advanced local densification was observed after the experiments at 10%RH.

Figure 8. Photographs extracted from the video of sample RH50-b during the last 5 s of the voltage ramp with a slope of 25 V s⁻¹ applied at 35°C.



Figure 9. SEM micrographs of the RH90-a pellet after the partial discharges experiments. The top micrograph shows the location at the edge of the face that was next to the grounded electrode. The bottom micrographs are higher magnification micrographs of two zones, showing the local surface densification into large hexagonal grains.



4. Discussion

Based on the PD patterns and the video recordings of the experiments conducted at different levels of RH, significant differences can be pointed out in the types of electric discharges. At 10%RH, the majority of discharges was found to be electric arcs between electrodes, which were strongly correlated with high amplitude PDs (~1000 pC), mainly in the negative polarity. At 50%RH, the amplitude of the PDs was significantly lower, and electric discharges were visible at the interfaces between the sample and the electrode, or at the triple junctions 'ZnO-platinum-air', rather than between the electrodes. At 90%RH, the maximum amplitude of the PDs was even lower (< 100 pC), and no visible electric discharges were observed. In short, the increase in RH led to a sharp reduction in the amplitude of PDs while increasing their number significantly.

One noteworthy observation is that, despite PDs having significantly greater amplitudes at 10%RH (several orders of magnitude) in comparison to 50%RH or 90%RH, these conditions did not lead to any visible traces on the sample after the experiments. This suggests that the arcs between the electrodes did not generate enough heat to increase the sample electrical conductivity, and thus, no conductive channel was formed in parallel inside the sample to divert the electric current from the channel present in the surrounding air. In dry air, Naidis have shown [50] that the major cause of arc formation is the increased level of the electron detachment rate with time because of the accumulation of oxygen atoms and other active chemical species. At 50%RH, the number of PDs was much higher compared to 10%RH, although their amplitude was lower. In [51], it was shown that gas heating during the discharge pulse increases with humidity due to the rapid vibration-to-translation transitions of H₂O and the exothermicity of the OH formation. The arcs initially formed on the surface of the sample and caused sufficient heating to trigger a local surface flashover. Figure 8 reveals that the arc, which originally developed between the two electrodes, split into two smaller parts at each electrode, causing the central part of the arc to disappear at mid-height of the sample. These two portions of the arc moved on the sample surface. Such a behaviour contrasts with that of the initial arc which remained pinned to a specific location for its entire duration. In a recent study of flash sintering of ZnO at room temperature by Yan *et al* [52], abnormal grain growth was reported locally in areas near the triple junction where their silver electrodes, sample, and air were in contact. In the experiments reported here, the triple junction 'ZnO-platinum-air' was also found to be the location of numerous visible discharges at 50%RH as well as the space between the sample and the electrodes. We can infer that the exact location where the arcs are initiated are linked to any electric field enhancement in the system. Such enhancement can originate from the roughness of the metallic electrodes, open porosity of the external surface of the dielectric or charge accumulations. Several works have shown the strong influence of surface roughness on various physical mechanisms and, in particular in the electrical point of view, increased roughness was shown to lead to a reduced breakdown field [53]. This electric field enhancement was also studied by finite element modelling [54] which shows that maximum field strength magnifications can reach up to a factor of 4 when increasing the root-mean-squared amplitude roughness from 0 μm to 0.16 μm at the interface between the ceramic and the electrode in ceramic capacitors. Li *et al* [55] proposed the use of an extra tip in the

electrode design to enhance the electric field and induce local surface flashover, resulting in flash sintering of their ZnO dog-bones. A comparable mechanism based on surface flashover was proposed by Zhu *et al* [56] as an induction mechanism for flash sintering of three YSZ at room temperature: depending on the experimental parameters, the electric arc, which generated high temperatures and was suspended over the sample, was observed to either remain detached from the sample throughout the experiment or eventually heat the upper surface of the sample. This led to an increase in conductivity, resulting in densification from the upper surface to the internal volume of the sample [56].

Hensel *et al* conducted several studies on the generation of microdischarges in porous ceramics using DC [57, 58] or AC [59, 60] HV. In the AC field, they studied the effects of pore size, discharge power, gas mixture, and water vapour on the discharge properties and development. Their results showed that the onset voltage of the microdischarges decreased with increasing pore size and that the amplitude of the discharges increased with the applied voltage, pore size, and oxygen content [59]. The effect of water vapour was also significant [60]: with increasing humidity, first a decrease of the onset voltage of the capillary microdischarges caused by the increased conductivity of the ceramics was observed, followed by an increase caused by the electron scavenging effect. The significant increase of the volume DC and AC conductivity at 50 Hz in our green ZnO samples (figure 2) gives a clear signature of water absorption when the RH increases. The possible impact is that the current that flows within the sample should be larger when the RH is increased. The electric arcs, if any, would therefore be located within the sample rather than passing in the air from one electrode to the other.

In our work, at a RH of 90%, we did not observe any bright arc resulting from surface flashover between the electrodes, and the electric discharges at the triple point where the interface of the electrode-sample-air meets were barely noticeable. The discharges were characterized as a large number of PDs of small amplitude, rather than rare PDs of high amplitude or complete arcs between the electrodes. Based on studies from the literature, a possible scenario can be proposed. The constant generation of small electric discharges could be associated with a more gradual heating of the sample or even sustain electrochemical reactions. In addition to a continuous generation of mobile ions, these electrochemical reactions have been reported to create chemical species like O_3 and NO_x [61, 62], especially at high RH [38]: N_2 and O_2 from the air can react with humidity to form hydroxyl radicals ($\cdot OH$), hydrogen peroxide (H_2O_2) or acidic compound such as HNO_3 that can dissolve the sample surface and form a superficial layer of soluble zinc nitrate that increases the surface conductivity. The increase of the surface conductivity would in return impact the occurrence of subsequent PDs as it would help in removing the space charges of preceding discharges [24]. Another known effect of increased RH is a reduction of the concentration of free electrons in the air [36, 37] because of the electronegative nature of water vapour and a lower mobility of the subsequently formed ions clusters. The PD behaviour observed here in figure 4(b) can be put in relation with PD patterns obtained on the metal-dielectric air gap in machine insulation [37], for which the PD amplitude is also reduced greatly while their average number increased dramatically with the increasing humidity.

In the context of flash sintering of zinc oxide, possibly close to room temperature as reported by Nie *et al* [19], our impedance spectroscopy measurements confirm an increase in the electrical conductivity of the sample by several orders of magnitude in high RH. Various effects where water could aid in the transport of mass were reported by Gonzalez-Julian *et al* [63] in the cold sintering of ZnO: H⁺ [64] and OH⁻ ions can diffuse under high electric field and be trapped at the grain boundaries up to 400°C [65], and the dissolution-precipitation of Zn²⁺ and O²⁻ ions [66] can contribute to a reduction in the activation energy of atomic diffusion due to the formation of defects at the grain boundaries. Surface-bound hydroxide ions enhance surface diffusion and can promote pore coalescence [67], green sample densification [40] and texture development [68], thus playing a crucial role in enhancing the sintering process in ZnO. These mechanisms and our PD measurements emphasize the significant effect of RH in the densification of ZnO samples at low temperature and high electric field. This requires careful consideration when researching the most reliable flash sintering process while also reducing energy consumption.

5. Conclusion

When Zhou *et al* [20] recently reviewed the challenges of flash sintering using a strong electric field, they emphasised the need to develop advanced techniques for detecting and observing electric discharges in high electric field flash sintering experiments to obtain quantitative data and improve our understanding in this field. In this work, we have demonstrated that the PRPD technique is able to identify distinct regimes of electric discharges.

The evolution of PD patterns with increasing AC voltage presented different characteristics that could be attributed to various locations on the porous sample, at its surface, or at the interface with the electrodes. Two distinguishable types of PDs with varying inception thresholds could be identified, where the first type exhibited a strong correlation with humidity levels, while the second type showed a considerably weaker dependence. The latter correspond to the appearance of PD clusters happening in a very narrow phase window of 10° called 'vertical cluster' which, at RH = 10%, was unambiguously attributed, through video recordings, to the occurrence of brief high-amplitude electric arc between the Pt electrodes. The number of these PDs is relatively low and, at higher electric fields, the majority of the observed PDs appears mostly at the triple junction 'ZnO-platinum-air' or within the ZnO- electrode gap.

As RH increases, the number of PDs increases while their maximum amplitude decreases strongly. At RH = 50%, a large number of low-amplitude PDs are mainly located at the triple junction 'ZnO-platinum-air' or at the interface between the electrodes and the sample. The vertical clusters are still measured in the PD pattern acquisition but, as their amplitude is lower, they are not visible on the video recording of the experiment. At the investigated highest humidity level (RH = 90%), almost no optical event can be observed, although the number of discharges is definitely the highest. This finding confirms that the presence of water vapour in the atmosphere, absorbed in the volume of the sample (confirmed by volume conductivity measurement) or adsorbed at its

surface, can have a significant impact on the flash sintering process at room temperature under high electric fields.

DATA AVAILABILITY STATEMENT

All data that support the findings of this study are included within the article (and any supplementary files).

ACKNOWLEDGMENTS

This study is supported by ERDF and the Walloon Region, in the frame of IMAWA—FLASHSINT research project (program 2014-2020).

CONFLICT OF INTEREST

The authors have no conflicts of interest to disclose.

APPENDIX. PRELIMINARY RESULTS ON PTFE

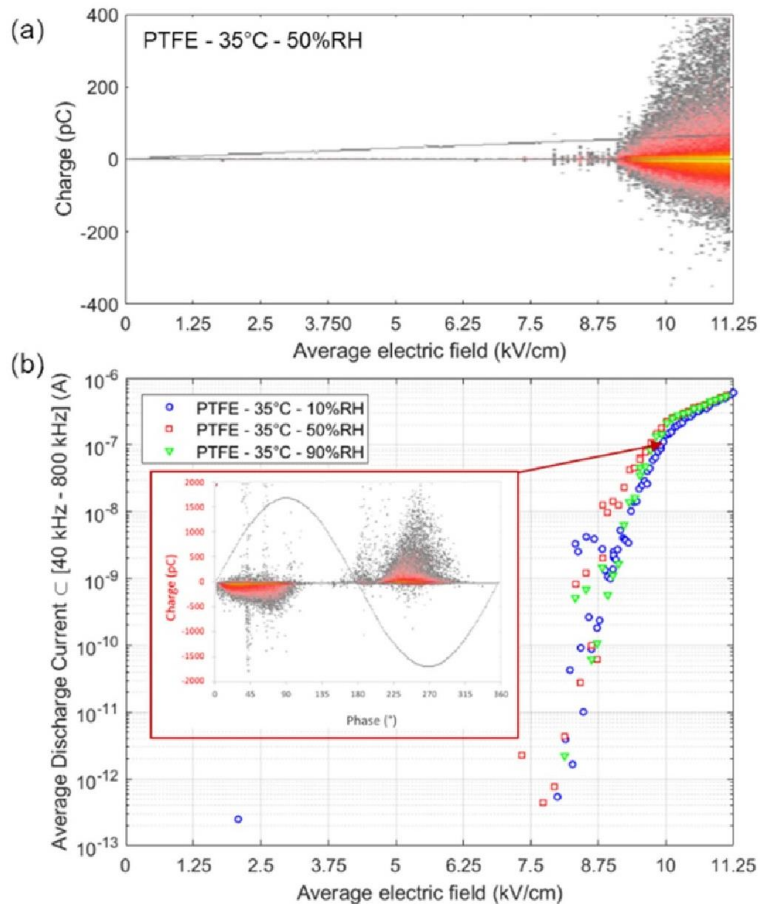
We investigated the PD behaviour on PTFE samples of dimensions similar to ZnO (thickness = 5 mm, diameter = 8.2 mm). Compared to a ZnO ceramic, PTFE has no pores, which eliminates PDs appearing in internal voids. The flat surfaces of PTFE in contact with the platinum electrodes being softer than the ceramic, the effective contact surface was larger and the electrode-sample interfaces were much less likely to be the site of PDs.

In a first experiment, the PTFE sample was subjected to a linear voltage ramp at 25 V s^{-1} (corresponding to the grey line in figure A1(a)), at 35°C and different RH levels, and the apparent charge was measured regardless to the phase in order to display the amplitude of the PDs and their inception voltage. Figure A1(a) presents results obtained at 35°C and 50%RH. No PDs could be observed below 8 kV cm^{-1} . Then sporadic low amplitude PDs were recorded followed by PDs of larger amplitude that increased almost linearly with the applied voltage.


PRPDs patterns were recorded during 30 s for increasing values of the average electric field up to 11.25 kV cm^{-1} . Figure A1(b) shows the evolution of the average discharge current with the average electric field for PTFE measured at 35°C and 10%RH, 50%RH and 90%RH. The curves appear to be similar for all values of the RH with a threshold of 10 pA occurring around 8 kV cm^{-1} . An example of the individual patterns, corresponding to the measurement of PTFE at 35°C , 50%RH and 10 kV cm^{-1} , is shown as inset of figure A1(b).

The conclusion of this experiment is that no PD was detected below 8 kV cm^{-1} when a PTFE sample with dimensions similar to those of the ZnO samples (see table 1) is placed in the same experimental conditions.


Figure A1. Experimental results obtained on a PTFE cylinder (thickness = 5 mm, diameter = 8.2 mm) at 35°C. (a) Amplitude of the partial discharges measured on the sample subjected to a linear voltage ramp at 50%RH. (b) Average discharge current calculated from partial discharged patterns measured at increasing values of the average electric field up to 11.25 kV cm⁻¹ at 10%, 50% and 90%RH. Inset: PRPD pattern obtained at 50%RH and 10 kV cm⁻¹.





ORCID IDS


Jean-François Fagnard  <https://orcid.org/0000-0002-8898-0298>


Laurent Boilet  <https://orcid.org/0000-0003-0579-7250>

Jean-Pierre Erauw  <https://orcid.org/0000-0001-5983-0349>

François Henrotte  <https://orcid.org/0000-0003-1578-1367>

Christophe Geuzaine  <https://orcid.org/0000-0001-9970-358X>

Bénédicte Vertruyen  <https://orcid.org/0000-0002-0128-7862>

Philippe Vanderbemden  <https://orcid.org/0000-0002-1436-7116>

References

- [1] Greuter F 2021 ZnO varistors: from grain boundaries to power applications *Oxide Electronics* ed A Ray ([https://doi.org/ 10.1002/9781119529538.ch8](https://doi.org/10.1002/9781119529538.ch8))
- [2] Wu A, Zhu Z, Wang X, Yan N, Zhou H, Huang R, Ma G, Jia Z and Wang L 2022 High-performance ZnO varistor ceramics prepared by arc-induced flash sintering with low energy consumption at room temperature *High Volt.* **7** 222-32
- [3] Meng P, Yuan C, Xu H, Wan S, Xie Q, He J, Zhao H, Hu J and He J 2020 Improving the protective effect of surge arresters by optimizing the electrical property of ZnO varistors *Electr Power Syst. Res.* **178** 106041
- [4] Meng F-B, Chen X, Shi Y, Hong Z, Zhu H, Muhammad A, Paramane A, Wang Y, Huang R and Deng X 2022 Spraying core-shell ZnO to achieve high insulation performance for HVDC cable factory joints *ACS Appl. Energy Mater.* **5** 7681-91
- [5] Yang X, Zhao X, Li Q, Hu J and He J 2018 Nonlinear effective permittivity of field grading composite dielectric *J. Phys. D: Appl. Phys.* **51** 075304
- [6] Cologna M, Rashkova B and Raj R 2010 Flash sintering of nanograin zirconia in <5 s at 850 °C *J. Am. Ceram. Soc.* **93** 3556-9
- [7] Biesuz M and Sglavo V M 2019 Flash sintering of ceramics *J. Eur Ceram. Soc.* **39** 115-43
- [8] Schmerbauch C, Gonzalez-Julian J, Röder R, Ronning C and Guillon O 2014 Flash sintering of nanocrystalline zinc oxide and its influence on microstructure and defect formation *J. Am. Ceram. Soc.* **97** 1728-35
- [9] Charalambous H, Jha S K, Christian K H, Lay R T and Tsalalagos T 2018 Flash sintering using controlled ramp *J. Eur. Ceram. Soc.* **38** 3689-93
- [10] Nie J, Zhang Y, Chan J M, Jiang S, Huang R and Luo J 2017 Two-step flash sintering of ZnO: fast densification with suppressed grain growth *Scr. Mater.* **141** 6-9
- [11] Liang Y, Xiang S, Li T, Yu C, Leng K and Zhang X 2021 Pressure-assisted flash sintering of ZnO ceramics *J. Am. Ceram. Soc.* **104** 6131-43
- [12] Phuah X L, Yang B, Charalambous H, Tsakalagos T, Zhang X and Wang H 2021 Microstructure and defect gradients in DC and AC flash sintered ZnO *Ceram. Int.* **47** 28596-602
- [13] Storion A G, Ferreira J A, Maestrelli S C and Maria de Jesus Agnolon Pallone E 2021 Influence of the forming method on flash sintering of ZnO ceramics *Ceram. Int.* **47** 965-72
- [14] Zhang Y and Luo J 2015 Promoting the flash sintering of ZnO in reduced atmospheres to achieve nearly full densities at furnace temperatures of < 120°C *Scr. Mater.* **106** 26-29
- [15] Wang X, Zhu Y, Huang R, Mei H and Jia Z 2019 Flash sintering of ZnO ceramics at 50°C under an AC field *Ceram. Int.* **45** 24909-13
- [16] Liu J, Li X, Wang X, Huang R and Jia Z 2020 Alternating current field flash sintering 99% relative density ZnO ceramics at room temperature *Scr. Mater.* **176** 28-31

- [17] Zhou H, Li X, Huang R, Yan N, Wang X and Jia Z 2021 Effect of atmospheric conditions on the onset electric field of ZnO and Y₂O₃ ceramics flash sintering at room temperature *Ceram. Int.* **47** 34068-71
- [18] Yan N, Pan J, Deng Z, Cai M, Zhao X, Liu J, Wang X and Jia Z 2022 Ethanol-induced flash sintering of ZnO ceramics at room temperature *Materials* **15** 862-70
- [19] Nie J, Zhang Y, Chan J M, Huang R and Luo J 2018 Water-assisted flash sintering: flashing ZnO at room temperature to achieve ~98% density in seconds *Scr. Mater.* **142** 79-82
- [20] Zhou H, Li X, Zhu Y, Liu J, Wu A, Ma G, Wang X, Jia Z and Wang L 2022 Review of flash sintering with strong electric field *High Volt.* **7** 1-11
- [21] Huang Z, Yang X, Yuan Z, Sun G, Sun Y, Hu J and He J 2022 The degradation of silicone rubber composites with ZnO microvaristors under impulse voltage *J. Phys. D: Appl. Phys.* **55** 355501
- [22] Hossam-Eldin A A 1984 Analysis of discharge damage and breakdown in gaseous cavities in insulating materials *J. Phys. D: Appl. Phys.* **17** 421
- [23] Kantar E and Hvidsten S 2021 A deterministic breakdown model for dielectric interfaces subjected to tangential electric field *J. Phys. D: Appl. Phys.* **54** 295503
- [24] Temmen K 2000 Evaluation of surface changes in flat cavities due to ageing by means of phase-angle resolved partial discharge measurement *J. Phys. D: Appl. Phys.* **33** 603
- [25] Korobeynikov S M, Ovsyannikov A G, Ridel A V and Karpov DI 2018 Study of partial discharges in bubbles and microsphere in transformer oil *J. Phys.: Conf. Ser* **1128** 012118
- [26] Hori T, Yanaze N, Kozako M, Hikita M, Wada J and Okabe S 2015 Partial discharge characteristics of epoxy composite with micro-meter size hollow glass particles *IEEE Conf. on Electrical Insulation and Dielectric Phenomena (CEIDP)* pp 366-9
- [27] Suwarno, Suzuoki Y, Komori F and Mizutani T 1996 Partial discharges due to electrical treeing in polymers: phase-resolved and time-sequence observation and analysis *J. Phys. D: Appl. Phys.* **29** 2922-31
- [28] Zhang R, Zhang Q, Zhou J, Guo C, He X, Wu Z and Wen T 2022 Critical study of partial discharge inception in voids: statistical behavior to stochastic nature *J. Phys. D: Appl. Phys.* **55** 065501
- [29] Song B, Ren M, Zhang Z, Zhuang T, Zhang C and Dong M 2020 Excess conduction induced by partial discharge in polymer *J. Phys. D: Appl. Phys.* **53** 485302
- [30] Bayer C F, Waltrich U, Soueidan A, Baer E and Schletz A 2016 Partial discharges in ceramic substrates—correlation of electric field strength simulations with phase resolved partial discharge measurements *Int. Conf. on Electronics Packaging (ICEP)* pp 530-5
- [31] Vu T A T, Augé J, Lesaint O and Do M T 2010 Partial discharges in aluminium nitrite ceramic substrates *10th IEEE Int. Conf. on Solid Dielectrics (ICSD)* pp 1-4
- [32] Shin B-C, Kim S-C, Nahm C-W and Jang S-J 2001 Nondestructive testing of ceramic capacitors by partial discharge method *Mater Lett.* **50** 82-86
- [33] Hang T, Glaum J, Phung T and Hoffman M 2014 Investigation of partial discharge and fracture strength in piezoelectric ceramics *J. Am. Ceram. Soc.* **97** 1905-11
- [34] Hang T, Glaum J, Genenko Y A, Phung T and Hoffman M 2016 Investigation of partial discharge in piezoelectric ceramics *Acta Mater.* **102** 284-91

- [35] Fagnard J-F, Gajdowski C, Boilet L, Henrotte F, Geuzaine C, Vertruyen B and Vanderbemden P 2021 Use of partial discharge patterns to assess the quality of sample/electrode contacts in flash sintering *J. Eur. Ceram. Soc.* **41** 669-83
- [36] Levesque M, David E, Hudon C and Belec M 2012 Contribution of humidity to the evolution of slot partial discharges *IEEE Trans. Dielectr Electr Insul.* **19** 61-75
- [37] Wang X, Taylor N and Edin H 2016 Effect of humidity on partial discharge in a metal-dielectric air gap on machine insulation at trapezoidal testing voltages *J. Electrostat.* **83** 88-96
- [38] Kourdi M B, Bui A, Loubiere A and Khedim A 1992 Behaviour of metal-oxide-based varistors subjected to partial discharges in air *J. Phys. D: Appl. Phys.* **25** 548-51
- [39] Herrán J, Fernández I, Ochoteco E, Cabañero G and Grande H 2014 The role of water vapour in ZnO nanostructures for humidity sensing at room temperature *Sens. Actuators B* **198** 239-42
- [40] Dargatz B, Gonzalez-Julian J, Bram M, Jakes P, Schade L, Röder R, Ronning C and Guillon O 2015 FAST/SPS sintering of nanocrystalline zinc oxide—part I: enhanced densification and formation of hydrogen-related defects in presence of adsorbed water *J. Eur Ceram. Soc.* **36** 1207-20
- [41] Jha S K, Phuah X L, Luo J, Grigoropoulos C P, Wang H, García E and Reeja-Jayan B 2019 The effects of external fields in ceramic sintering *J. Am. Ceram. Soc.* **102** 5-31
- [42] ICMsystem from Power Diagnostix *Power Diagnostix Systems GmbH Homepage* (available at: <https://pdix.com/>)
- [43] Jonscher A K 1992 The universal dielectric response and its physical significance *IEEE Trans. Electr Insul.* **27** 407-23
- [44] Edwin Suresh Raj A M, Mallika C, Swaminathan K, Sreedharan O M and Nagaraja K S 2002 Zinc(II) oxide-zinc(II) molybdate composite humidity sensor *Sens. Actuators B* **81** 229-36
- [45] Pollak M 1971 On the frequency dependence of conductivity in amorphous solids *Phil. Mag. A* **23** 519-42
- [46] Elliott S R 1977 A theory of ac conduction in chalcogenide glasses *Phil. Mag. A* **36** 1291-304
- [47] Pike G E 1972 AC conductivity of scandium oxide and a new hopping model for conductivity *Phys. Rev. B* **6** 1572-80
- [48] Leonov S B, Adamovich I V and Soloviev V R 2016 Dynamics of near-surface electric discharges and mechanisms of their interaction with the airflow *Plasma Sources Sci. Technol.* **25** 063001
- [49] Moreau E 2007 Airflow control by non-thermal plasma actuators *J. Phys. D: Appl. Phys.* **40** 605-36
- [50] Naidis G V 1999 Simulation of streamer-to-spark transition in short non-uniform air gaps *J. Phys. D: Appl. Phys.* **32** 2649-54
- [51] Komuro A and Ono R 2014 Two-dimensional simulation of fast gas heating in an atmospheric pressure streamer discharge and humidity effects *J. Phys. D: Appl. Phys.* **47** 155202
- [52] Yan N, Deng Z, Cai M, Li X, Zhou H, Wang X and Jia Z 2021 Flash sintering of ZnO ceramics at room temperature with bisectonal electrode distributions *IEEE Conf. on Electrical Insulation and Dielectric Phenomena (CEIDP)* 422-5

- [53] Song G, Wang Y and Tan D Q 2022 A review of surface roughness impact on dielectric film properties *IET Nanodielectr* **5** 1-23
- [54] Heath J P, Harding J H, Sinclair D C and Dean J S 2019 Electric field enhancement in ceramic capacitors due to interface amplitude roughness *J. Eur. Ceram. Soc.* **39** 1170-7
- [55] Li X, Huang R, Wang X, Liu G, Jia Z and Wang L 2020 A simple optimized design of an electrode to conduct flash sintering at room temperature and low onset electric field *Scr. Mater* **186** 158-62
- [56] Zhu Y, Zhou H, Huang R, Yan N, Wang X, Liu G and Jia Z 2022 Gas-discharge induced flash sintering of YSZ ceramics at room temperature *J. Adv. Ceram.* **11** 603-14
- [57] Hensel K, Matsui Y, Katsura S and Mizuno A 2004 Generation of microdischarges in porous materials *Czech. J. Phys.* **54** C683
- [58] Hensel K, Katsura S and Mizuno A 2005 DC microdischarges inside porous ceramics *IEEE Trans. Plasma Sci.* **33** 574-5
- [59] Hensel K, Martisovits V, Machala Z, Janda M, Lestinsky M, Tardiveau P and Mizuno A 2007 Electrical and optical properties of AC microdischarges *Porous Ceram. Plasma Proc. Polym.* **4** 682-93
- [60] Hensel K and Kim H 2009 Effect of noble gases and water vapour on discharge in porous ceramics *19th Int. Symp. on Plasma Chemistry* pp 1-4
- [61] Sakiyama Y, Graves D B, Chang H W, Shimizu T and Morfill G E 2012 Plasma chemistry model of surface microdischarge in humid air and dynamics of reactive neutral species *J. Phys. D: Appl. Phys.* **45** 425201
- [62] Gao F, Wang Q, Dai D, Ning W, Zhang Y and Li L 2020 Numerical study on partial discharge in a dry air cavity with a two-dimensional fluid model considering practical reactions *J. Phys. D: Appl. Phys.* **53** 345202
- [63] Gonzalez-Julian J, Neuhaus K, Bernemann M, Pereira da Silva J, Laptev A, Bram M and Guillon O 2018 Unveiling the mechanisms of cold sintering of ZnO at 250°C by varying applied stress and characterizing grain boundaries by kelvin probe force microscopy *Acta Mater.* **144** 116-28
- [64] Doh W H, Roy P C and Kim C M 2010 Interaction of hydrogen with ZnO: surface adsorption versus bulk diffusion *Langmuir* **26** 16278-81
- [65] Dargatz B, Gonzalez-Julian J and Guillon O 2015 Anomalous coarsening of nanocrystalline zinc oxide particles in humid air *J. Cryst. Growth* **419** 69-78
- [66] Jabr A, Fanghanel J, Fan Z, Bermejo R and Randall C 2023 The effect of liquid phase chemistry on the densification and strength of cold sintered ZnO *J. Eur Ceram. Soc.* **43** 1531-41
- [67] Varela J A, Whittemore O J and Longo E 1990 Pore-size evolution during sintering of ceramic oxides *Ceram. Int.* **16** 177-89
- [68] Dargatz B, Gonzalez-Julian J, Bram M, Shinoda Y, Wakai F and Guillon O 2016 FAST/SPS sintering of nanocrystalline zinc oxide—part II: abnormal grain growth, texture and grain anisotropy *J. Eur Ceram. Soc.* **36** 1221-32